Microstructure morphology of chemical and structural phase separation in thermally treated $K_xFe_{2-y}Se_2$

G. Campi[1], G. Tommasucci[2], M. Tanaka[3,4], H. Takeya[3], Y. Takano[3], A. ESRF[5], T. Mizokawa[6] and N.L. Saini[2]

[1]Institute of Crystallography, CNR, via Salaria Km 29.300, I-00015 Monterotondo Roma, Italy

[2]Dipartimento di Fisica, Universitá di Roma "La Sapienza" - P. le Aldo Moro 2, I-00185 Roma, Italy

[3]MANA, National Institute for Materials Science, 1 2 1 Sengen, Tsukuba, Ibaraki 305 0047, Japan

[4]Graduate School of Engineering, Kyushu Institute of Technology, 1-1 Sensui-cho, Kitakyushu 804-8550, Japan

[5]European Synchrotron Radiation Facility (ESRF), 71, avenue des Martyrs, 38043 Grenoble Cedex 9, France

[6]Department of Applied Physics, Waseda University, Tokyo 169-8555, Japan

Abstract

The iron-based superconductor $K_xFe_{2-y}Se_2$ displays chemical, structural and electronic phase separation at nano to microscale, leading to the coexisting metallic phase embedded in an antiferromagnetic host matrix. The metallic phase is believed to arise from a percolative granular network, affecting transport in the normal as well as in the superconducting state. This percolative network can be manipulated and controlled through thermal treatments. In this study, we have used scanning X-ray micro-fluorescence to visualize different morphology due to phase separation coupled with percolation manipulated by two distinct thermal treatments, i.e., fast quenching and slow cooling of $K_xFe_{2-y}Se_2$. We find a differing negative spatial correlation between Fe and K distributions in the differently treated samples, ascribed to a different degree of Fe vacancy ordering. We have also identified an intermediate phase that acts as an interface between the two main phases. The high temperature quenching produces directionally oriented clustered microstructure in which the percolation threshold is lower and hence a more effective network for the transport pathways. Instead, the slow cooling results in larger interfaces around the percolation threshold that seems to affect the superconducting properties of the system. The results provide a quantitative characterization of microstructural morphology of differently grown $K_xFe_{2-y}Se_2$ showing potential for the design of advanced electronic devices based on sub-micron scale chemical phase separation, thus opening avenues for further studies of complex heterogeneous functional structures.

Introduction

Phase separation is a common phenomenon in many materials [Skolnick, 2024], including high-temperature superconductors [Campi, 2013; Campi, 2021, Wen, 2000; Fine, 2008]. Among others, $K_xFe_{2-y}Se_2$ [Yan, 2012] is a model compound in which the electronic and structural phase separation is known to be associated with the nano-scale chemical inhomogeneity. Indeed, alongside differing K and Fe concentrations in $K_xFe_{2-y}Se_2$ a clear structural and electronic phase separation into minority paramagnetic (PAR) metallic granular phase and majority antiferromagnetic (AFM) matrix has been observed through various experimental techniques, including X-ray diffraction [Ricci, 2015; Ricci, 2020; Shoemaker, 2012; Louca, 2013], transmission electron microscopy [Li, 2012], magnetic susceptibility measurements [Yan, 2012], μ-ARPES [Bendele, 14; Chen, 2021] and others [Simonelli, 2014].

The interplay between phase separation and transport properties in $K_xFe_{2-y}Se$ has been the subject of numerous studies [Zheng, 2012]. Concerning superconductivity, one proposed mechanism is that the metallic phase, exhibiting strongly dispersive bands near the Fermi level, forms percolative networks allowing for the efficient transport of Cooper pairs [Ding, 2013]. The thermal treatment through the vacancy ordering temperature T_s ~ 270°C [Yanagisawa, 2017] can change locally the elemental distribution and content, consequently the weight of the PAR and AFM phases at different length scale. As a result, different microstructures can be built, with the occurrence of an intermediate phase acting as interface between the two phases. The possibility to manipulate the microstructural morphology will allow to tune transport properties of this granular texture with a better understanding of the relationship between its microstructure, superconductivity and the normal state.

Here, we have used scanning X-ray micro-fluorescence measurements to map the elemental content in two $K_xFe_{2-y}Se_2$ samples subjected to two different thermal treatments: a fast quenched and a slow cooled sample. The different morphological textures in differing thermal treatments have been quantified by physical and spatial statistical tools such as cluster analysis to visualize percolation pathways of forming clusters with the evolution of the two phases as a function of the Fe content. This offers a possibility to realize new advanced electronic devices based on the submicrometric chemical phase separation [Abd Mutalib, 2018; Ma, 2016]. While this study focused on $K_xFe_{2-y}Se_2$, similar systematic characterizations could be applied to other phase-separated materials to unravel the role of microstructural morphology in their properties.

Results

2.1 Scanning nano X Ray Fluorescence measurements

We have performed spatial mapping of the Fe, K and Se elements within the volume of $K_xFe_{2-y}Se_2$ crystals using scanning X-ray micro-fluorescence. Spatially averaged X-ray fluorescence profiles obtained on the quenched and slow-cooled samples are shown in **Figure 1a** and **Figure 1b**. For each 0.3x0.3 μm^2 spot of the maps we have collected an XRF profile. In each normalized profile we have calculated the elemental content in the sample as given by the integrated intensity of the Fe, K and Se fluorescence peaks, indicated by the shadowed areas, for the slow cooled and quenched samples (see Methods section for experimental details).

2.2 Spatial distribution of Fe and K.

The spatial elemental distribution maps and the Probability Density functions (PDF) of Fe are shown in **Figure 2a** and **Figure 2b**. Similarly, the spatial distribution maps and PDFs of K distribution are shown in **Figure 2c** and **Figure 2d**. Mean and the standard deviations of both Fe and K distributions are reported in table 1 and table 2. We can observe a larger distribution of Fe and K in the slow cooled sample due to lower contents of these two elements. The PDFs follow

an abnormal line shape deviating from the normal distribution. We have used *the t-location-scale* distribution and by the *Generalized Extreme Value* distribution [Taylor, 2016] to model heavy tails in the K distribution and in the Fe distribution. Here, the heavy distribution is characterized by the decay slower than an exponential function. Heavy-tailed distributions are characterized by many small events and a limited number of large events giving rise to spatial patterns emerging due to interaction between different components in complex systems, as found in several research fields [Su, 2004; Campi 2017; Nair, 2022; Klebanov, 2023;]. The *t-location-scale* distribution is characterized by a location parameter, μ_K, a scale parameter σ_K, and a shape parameter, v_K. The shape parameter plays a crucial role in determining the behavior of the tail. The distribution tends to the normal distribution as v_K approaches infinity, while smaller values of v_K yield heavier -tailed distribution. The *Generalized Extreme Value* distribution combines three simpler distributions to model a continuous range of possible shapes [Kotz, 2000]. Also, in this case the distribution is characterized by a location parameter, μ_{Fe}, a scale parameter σ_{Fe}, and a shape parameter, k_{Fe}. The shape parameter, k, assumes negative values; as it approaches negative infinity, the upper bound of the distribution approaches the location parameter, μ, meaning that the distribution becomes increasingly concentrated around μ and the tail of decreases more rapidly to zero. On the other hand, if the k tends to zero from the negative side, the distribution approaches a Type I extreme value distribution, also known as the Gumbel distribution [Kotz, 2000], characterized by exponentially decreasing tail. Values of μ_{Fe}, σ_{Fe}, K_{Fe} and μ_K, σ_K, v_K are included in Table 1 and Table 2, respectively that can be compared with mean values $<C_{Fe}>$, $<C_K>$ and standard deviation values $\Delta(C_{Fe})$, $\Delta(C_K)$ extracted from Fe and K content maps.

2.3 Negative spatial correlation between Fe and K distributions: iron-vacancy order and interface phase

We should mention that in each measured spot a specific composition due to different contribution of PAR and AFM phases is found. The antiferromagnetic phase is an iron-vacancy-ordered phase with composition $K_{0.8}Fe_{1.6}Se_2$ (245) and space group *I4/m*, characterized by a $\sqrt{5}\times\sqrt{5}\times1$ superstructure and is believed to be responsible for the insulating behaviour of the material at low temperatures [Yeh, 2020]. The metallic phase with composition $K_1Fe_2Se_2$ (122) and space group *I4/mmm* is characterized by disordered iron-vacancies and is believed to be responsible for the superconductivity.

To visualize the phase separation between the two phases and to study the correlation of the same with the Fe and the K contents, we have introduced an empirical parameter defined as $\eta = C_{Fe}*C_K$. This parameter is normalized to have values ranging between 0-1 such that the 122-rich phase and the 245-rich phases correspond to η = 1 and 0 respectively. **Figure 3a** and **Figure 3b** display the normalized parameter η as a function of K and Fe. Incidentally, very few isolated spots contain stoichiometrically perfect 122 or 245 phases (i. e., η = 1 or η = 0). We have considered η>0.85 and η<0.15 to separate 122-rich and 245-rich regions, respectively. These regions are highlighted as shadowed areas. We expect to observe an increasing behavior of Fe and K content as a function of η from $C_{Fe}*C_K$ = 1.28 (η=0) in the 245-rich phase, where C_{Fe} = 1.6 and C_K = 0.8, to $C_{Fe}*C_K$ = 2 (η=1) in the 122-rich phase where C_{Fe}=2 and C_K=1. We can see that the K content follows this expected behavior, and in the 122-rich region it tends to the higher value ($C_K \approx 1$) in both samples unlike the Fe content that is lower than the optimum ($C_{Fe} \approx 2$) and distributes around C_{Fe} = 1.64. It can be easily judged that, on an average, both samples have Fe as well as K deficiency. The 122 phase is characterized by higher iron-vacancies than the 245 phase, however, they should be completely disordered in the earlier. Furthermore, the slow-cooled sample is characterized by a higher K deficiency than the quenched sample. It is also apparent that with the slow cooling the sample tends to move towards the 122-phase region. Therefore, unlike the expected higher Fe and K contents, the Fe-rich and K-rich regions in Fig. 3b do not correspond to regions where the contribution of the 122 phase is larger. At the origin of this behavior, it could be the occurrence of disordered vacancies and the depletion zones due to the interface between the 122 and 245 phases [Ricci, 2017]. This phase separation between the 122

and 245 phase with the occurrence of the intermediate interface is pictorially represented in **Figure 3c**. The interfaces can play a significant role in the phase separation, especially at the nanoscale. In fact, a clear reorganization of iron-vacancy order around the phase transitions has been observed, with the interface phase being mostly associated with a different iron-vacancy configuration [Duan, 2018]. This could be potentially important to assist the percolative superconductivity in $K_xFe_{2-y}Se_2$ [Liu, 2015; Ricci, 2015]. Therefore, it's plausible that the phase separation at an Fe content less than 2 can be affected by both the interface phase and vacancies content.

This unexpected behaviour causes the negative spatial correlation of the Fe distribution with the K distribution in both quenched and slow cooled samples. Indeed, the Pearson correlation coefficients [Kirch, 2008] between Fe and K spatial distribution are $c_{Fe,K}$ = -0.55 and -0.42 respectively in the quenched and the slow cooled samples, assuming this to be nearly 0 (no correlation) between the other pairs of elements, i.e., Fe and Se ($c_{Fe,Se}$) and K and Se ($c_{K,Se}$). This negative spatial correlation is illustrated in **Figure 3d**, by the scatter plot of K versus Fe content measured point by point in the distribution maps. We expect that the 122 PAR phase occurs when the Fe and K contents are both higher.

2.4 Chemical and structural phase separation coupled with percolation.

The different phase separation between the PAR 122 and AFM 245 phases with the development of different interface pathways, give rise to different granular morphology at microscale. The differing morphology in the two samples (quenched and slow cooled) has been characterized by studying the connectivity and the percolating pathways as a function of the Fe and K content using 2D cluster model analysis [Stauffer, 1994]. We have considered two adjacent pixels to be part of the same cluster if they are interconnected in the horizontal, vertical, or diagonal directions and have Fe (or K) content below a threshold value. In this way, we can calculate all the forming clusters, as a function of content and pick-out the cluster with the largest extent. The Fe content at which we find the first spanning cluster with size equal to the system size, gives the percolation threshold, P_T^{Fe}, of the system. To visualize the clusters formation with the occurrence of percolation pathways we show the binary maps at different ranges of Fe for the quenched (**Figure 4a)** and the slow cooled (**Figure 4b)** samples. Here the white pixels represent the presence of Fe relative to the indicated compositional range. The texture at which percolation occurs are indicated by the red and blue frames for the quenched and the slow cooled samples, respectively. Spanning cluster size and percolation thresholds, P_T^{Fe}, in quenched and slow cooled samples are shown in **Figure 4c**. We have found that the percolation threshold of P_T^{Fe} = 1.64 in the slow cooled sample is higher by ~2% than the P_T^{Fe} = 1.61 value in the quenched sample. These values correspond to the Fe content where we have found the larger contribution of the 122 phase in Figure 3. Thus, we can argue that the percolation at C_{Fe} = 1.61 in the quenched and C_{Fe}= 1.64 in the slow cooled samples represent a chemical-structural phase separation coupled with percolation [Zhou, 2012].

The percolation probability of the Fe- is given by $P_p^{Fe} = n_{occ}/N$ where n_{occ} and N are the number of occupied *sites* and total *sites* in the distribution maps. In the quenched sample we find P_p^{Fe} = 0.34, that results to be substantially lowered in comparison with the percolation probability in the slow cooled sample, i.e., P_p^{Fe} = 0.50. It is worth mentioning that the occupation at the percolation threshold in a random square lattice is 0.59 [Mendelson, 1999], indicating that the quenched sample may have more ordered texture, allowing to reach the percolation at significantly lower site occupation. This can be an indication that the slow cooling permits more internal changes to occur, leading to a greater variety of microstructural regions. This larger morphological inhomogeneity in the slow cooled sample seems to be consistent with the larger number of clusters with differing shape factor around the percolation threshold of Fe content, at $C_{Fe} \approx 1.64$.

The number of clusters as a function of Fe content are shown in **Figure 4d**. At the same time the area, A, and boundary length (BL) of forming clusters has been calculated to build a shape factor v_{SF}= BL / 4πA, shown in **Figure 4e**. Clusters' numbers with their shape factor are larger in the slow cooled sample around the percolation threshold P_T^{Fe}. Furthermore, we find more and shorter correlation distances in the slow cooled samples, as shown in the spatial correlation function G(r) of the Fe spatial distribution, in Figure 1 of SI. Thermal treatment does not seem to modify the clusters analysis of the K distribution, as shown in Figure 2 of SI. Indeed, we find that the percolation threshold of P_T^K = 0.66 is same with percolation probabilities of 0.33 and 0.39 for the K sites in the quenched and slow cooled samples.

The intermediate phase at the interface between the 122 and 245 phases (schematically presented in **Figure 3a** has been characterized by calculating the Euclidean Distance Transform, EDT, of binarized maps at different intervals of the Fe content (see **Figure 2 of SI**). The EDT gives the distance from each pixel in one phase to the nearest pixel in the other phase [Maurer, 2003]. The average value of the EDT map, namely T parameter, can give us an idea of the typical distance from the interface within the two phases. This parameter can be used to characterize the interface thickness that is shown in **Figure 4f**. We notice that around the percolation threshold P_T^{Fe} the T parameter is larger in the slow cooled sample indicating gradual evolution transition between the two phases.

2.5 Ordering and degree of the inhomogeneity controlled by thermal treatment.

One of the possible causes for a more ordered texture in the rapidly quenched sample, could be given by larger clusters formation with larger orientational degree of the Fe richer domains. The orientational degree of Fe distribution refers to the extent to which the Fe sites are aligned or ordered in a particular direction. Thus, we have studied the orientational degree of Fe distribution in the two samples by calculating the gradient of Fe maps, $\boldsymbol{\nabla} C_{Fe}$, describing the rate of change of the Fe content in the x and y directions [Gonzales, 1987, Poccia 2020]. The gradient magnitude is the Euclidean norm of the gradient vector, and it represents the magnitude of the spatial variation of the Fe content at each pixel. High gradient magnitudes indicate areas of the image with strong edges or texture, while low gradient magnitudes indicate areas with little change in Fe content (see Figure 4 of SI). The gradient orientation is the angle of the gradient vector with respect to the positive x-axis, and it represents the direction of the spatial variation of the Fe content at each pixel. In other words, the gradient magnitude and orientation represent how much the intensity of the image changes in different directions [Gonzales, 1987, Poccia 2020]. Gradient orientation maps of the quenched sample with its Probability Density Function are shown in **Figure 5a** and **Figure 5b** for the quenched and slow cooled samples. As orientational degree, ρ, we have considered the fraction of oriented sites in both samples given by $\rho = {A_{peaks}}/{A_{BKG}}$ where A_{peaks} and A_{BKG} are the area under the peaks and the under the constant background in the Probability Density Functions of the Gradient orientation maps. The PDF profile peaks have been deconvoluted by gaussian functions. We have obtained a larger orientational degree, ρ = 0.72, for the quenched sample, in comparison with 0.42 for the slow cooled sample, indicating a higher level of grain alignment of Fe sites, or higher texturing. Beyond the lower orientational degree, the slow cooled sample show also different orientations associated to the different peaks in the PDF involving smaller domains. The larger orientational degree of occupied Fe sites in the quenched sample plays a pivotal role in determining its more ordered and conductive microstructural morphology, resulting in a lower percolation threshold of Fe sites, associated with the percolation of the 122 phase. Rapid quenching tends to create thinner interfaces. These findings indicate that the rate of cooling has a significant impact on the microstructure and thus the functionality of the title compound [Park, 2002].

Summary and conclusions

We start our discussion by recalling that the present study is focused on the characterization of microstructural morphology of $K_xFe_{2-y}Se_2$, a material exhibiting phase separation with coexistence of minority metallic (PAR) and majority antiferromagnetic (AFM) phases. We have used scanning X-ray micro-fluorescence to map the elemental content in two samples subjected to different thermal treatments: fast quenching and slow cooling. We have found heavy-tailed distributions of Fe and K in the two samples revealing spatial organization with distinct morphological textures. Negative spatial correlation between Fe and K distribution is found in both samples. Cluster analysis allowed us to visualize the microstructural connectivity identifying percolating pathways due to metallic phase and the evolution of the interface between the Fe-rich and the Fe-poor insulating phase. The observation of a lower percolation probability in the quenched sample, compared to the slow cooled sample, suggests that the former exhibits a more ordered texture, allowing it to achieve percolation at a lower Fe site occupation. The difference in the ordering degree of microstructure is likely to be due to larger orientational degree of the Fe-rich domains in the quenched sample.

Understanding the mechanisms responsible for this difference in the orientational degrees could contribute to control the material's anisotropic properties. A higher orientational degree implies a more organized and interconnected network, making it easier for the metallic phase to form percolating clusters and establish efficient pathways for the charge transport. On the other hand, the lower orientational degree in the slow cooled sample suggests a less ordered arrangement of Fe sites, which may hinder the formation of well-connected metallic clusters. Consequently, the slow cooled sample requires a higher Fe site occupation probability to achieve the percolation, indicating a more disordered and less conductive network of metallic regions.

It appears that, by carefully controlling the cooling rate, is it possible to tune the inhomogeneity and the interface between the two phases. In the rapid quenching a more abrupt change between phases “freeze” the material structure in a high-energy state, leading to highly textured domains with thinner interface. On the other hand, slow cooling permits higher diffusion and can lead to domains with thicker interface.

It should be mentioned that the knowledge on the effect of the orientational degree on microstructural morphology and the percolation behavior is a crucial for control and manipulation of the transport properties of functional materials, especially granular systems exhibiting phase separation. By controlling the orientational degree through appropriate thermal treatments or synthesis techniques, researchers and engineers can manipulate the material's connectivity and conductivity, leading to the design of new electronic devices with desired performance characteristics.

Materials and Methods

X-ray fluorescence imaging was carried out at the ID21 beamline of European Synchrotron Radiation Facility (ESRF) in Grenoble. The Scanning X-ray Microscope at the ID21 permits to perform micro-X-ray fluorescence (μXRF) measurements with submicron resolution in the energy range of 2 – 9 keV [Cotte, 2017]. X-ray beam emitted by an undulator source is monochromatized a fixed-exit double-crystal Si(111) monochromators (Kohzu Precision Co. Ltd., Japan) with fixed-exit double-mirror systems for harmonic rejection delivering energy resolution $\Delta E/E = \sim 2\times10^{-4}$. The focusing optics uses multilayer Kirkpatrick-Baez (KB) mirror systems providing beam size down to 300x300 nm2. Fluorescence is detected by single-element Silicon Drift Diode detectors (Bruker XFlash 5100, 80mm^2 area). Spectra are collected in “zap” continuous scanning mode, by raster-scanning the sample in front of the focused beam while detectors continuously collect spectra. The primary beam energy was tuned to the main x ray absorption edge energy of Fe K-

edge. The μXRF maps were acquired with an incident beam energy of 7130 eV. The overview maps were obtained by scanning the sample with a 0.3 × 0.3 μm^2 step size. Data have been normalized considering the total compositional values, C_{TOT}, of Fe, K and Se measured by energy dispersive X-ray (EDX) spectroscopy [Tanaka, 2016, Yanagisawa, 2017] and reported in Table 1. The data were analyzed by using home-made MATLAB routines [Campi, 2019]. $K_xFe_{2-y}Se_2$ single crystals were prepared by quenching and slow cooling as described in [Tanaka, 2016].

Tables

Sample	$nC(Fe)_{AFM} + mC(Fe)_{PAR}$	$<C_{Fe}>$	$\Delta(C_{Fe})$	μ_{Fe}	σ_{Fe}	K_{Fe}	$R^1_{Fe}(\mu m)$	P_p^{Fe}	ρ_{Fe}
S	(9/10)*1.610 + (1/10)*1.945	1.64	0.07	1.61	0.07	-0.17	14	0.51	0.42
Q	(2/3)*1.608 + (1/3)*1.707	1.64	0.06	1.61	0.06	-0.11	26	0.34	0.72

Table 1 Compositional content C_{AFM} and C_{PAR} of Fe in the majority AFM and minority PAR phase in the slow cooled and quenched samples. The total content of Fe and K is given by $C_{TOT} = nC_{AFM} + mC_{PAR}$ where n and m represent the fraction of the two phases. We also report the mean content <C(Fe)> corresponding to C_{TOT} and the standard deviation, σ, of Fe and K distributions. We also report the correlation distance R_1, the percolation probability, P_p and the orientational degree ρ. Values of μ_{Fe}, σ_{Fe}, K_{Fe} represent the location, scale and shape parameters extracted by modelling the data with a Generalized Extreme Value distribution and can be compared with mean and standard deviation values of $<C_{Fe}>$, $\Delta(C_{Fe})$.

Sample	$nC(K)_{AFM} + mC(K)_{PAR}$	$<C_K>$	$\Delta(C_K)$	μ_K	σ_K	v_K	$R^1_K(\mu m)$	P_p^K	ρ_K
S	(9/10)*0.688 + (1/10)*0.395	0.66	0.08	0.66	0.08	34.61	12	0.39	0.58
Q	(2/3)* 0.698 + (1/3)* 0.627	0.67	0.06	0.67	0.06	13.47	12	0.34	0.38

Table 2 Compositional content C_{AFM} and C_{PAR} of K in the majority AFM and minority PAR phase in the slow cooled and quenched samples. The total content of K is given by $C_{TOT} = nC_{AFM} + mC_{PAR}$ where n and m represent the compositional ratio in the two phases. We also report the mean content $<C_K>$ corresponding to C_{TOT} and the standard deviation, σ, of K normal distributions. Values of μ_k, σ_k, v_k represent the location, scale and shape parameters extracted by modelling the data with a t located distribution and can be compared with mean and standard deviation values of $<C_{Fe}>$, $\Delta(C_{Fe})$.

Figures and figure captions

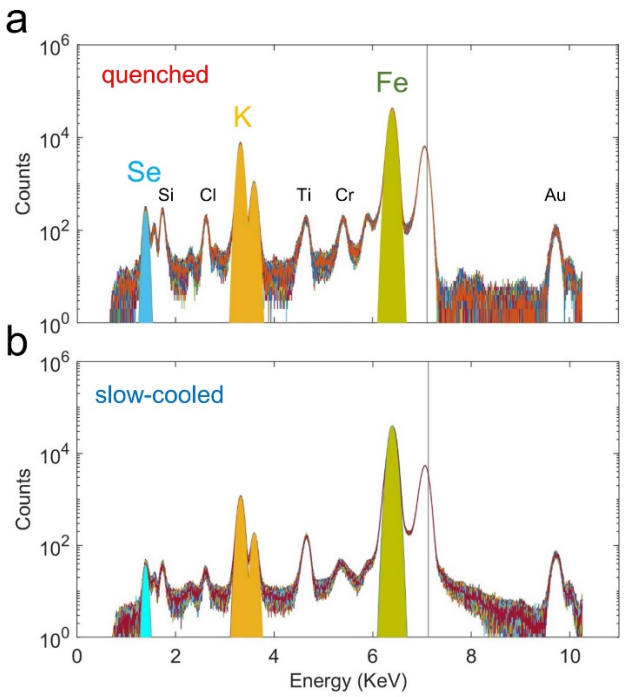

Figure 1. Scanning nano X Ray Fluorescence measurements.

Space averaged X-ray fluorescence profiles obtained by integrating from the map collected on the **(a)** quenched and **(b)** slow-cooled samples. The florescence maps were collected using incident photon energies of 7.1125 keV and 7.1308 keV for the quenched and slow cooled samples, respectively. The fluorescence peaks corresponding to the Fe Kα (~ 6.402 keV), K Kα (~ 3.313 keV) and Se Lα (~ 1.419 keV) are coloured shaded areas. For each 0.3x0.3 μm^2 spot we have collected an XRF profile and in each profile, we have calculated the integrated intensity of the Fe, K and Se peaks, associated to the elemental content in the sample.

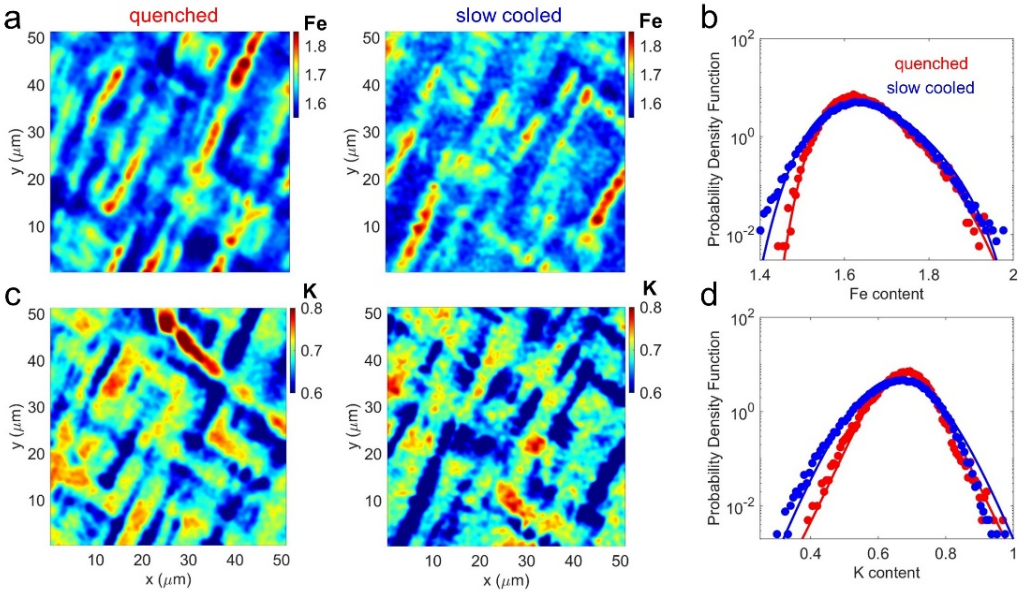

Figure 2. Spatial distribution of Fe and K content.

(a) Elemental distribution maps for Fe, in the quenched and slow cooled samples. **(b)** Probability Density Functions extracted from the fluorescence intensity maps in (a). Similarly, the K elemental distribution maps **(c)** and corresponding Probability Density Functions are shown in **(c)** and **(d)** for the quenched and slow cooled samples. The continuous lines in b) and d) represent the fits of the Probability Density Functions using the (b) *Generalized Extreme Value* and (d) *location-scale* distributions [Taylor, 2016]

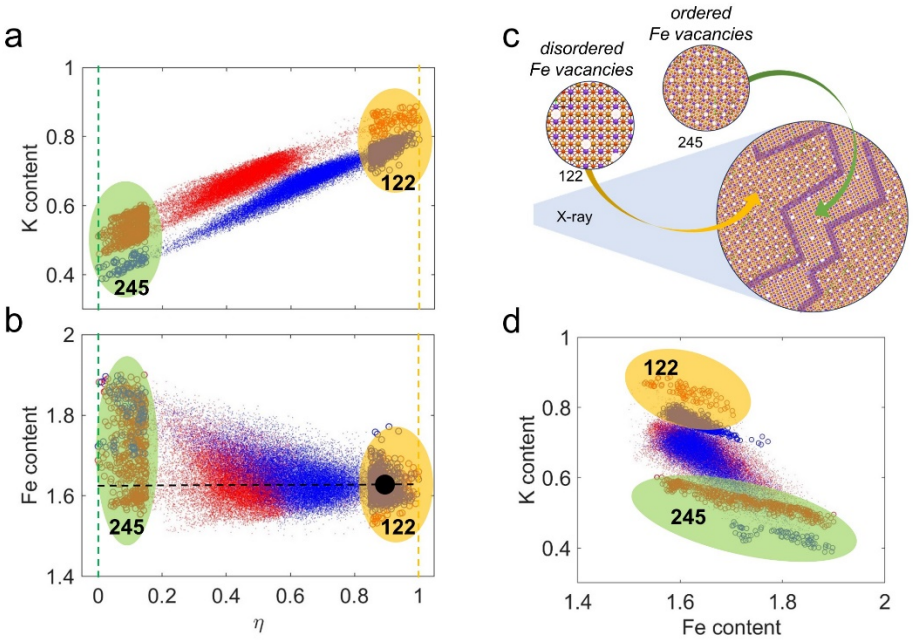

Figure 3. Negative spatial correlation between Fe and K distributions: reorganization of iron-vacancy order and interface phase

(a) K and **(b)** Fe content as a function of η (see text). The spots ($\eta>0.85$) are indicated by empty circles in the yellow shadowed areas, while the 245-rich regions ($\eta<0.15$) are indicated by empty circles in the green shadowed areas. The vertical dashed lines at $\eta=0$ and $\eta=1$ indicate the stoichiometrically perfect (green lines) 245 and (orange lines) 122 phases **(c)** Phase separation between the 122-rich and 245-rich phases is schematically presented together with an intermediate interface phase **(d)** Scatter plot of measured K versus Fe content, point by point, showing the negative spatial correlation between Fe-rich and K-poor zones in the quenched (red points) and slow cooled (blue points) samples. The negative corelations is quantified by Pearson coefficients, provided in the text.

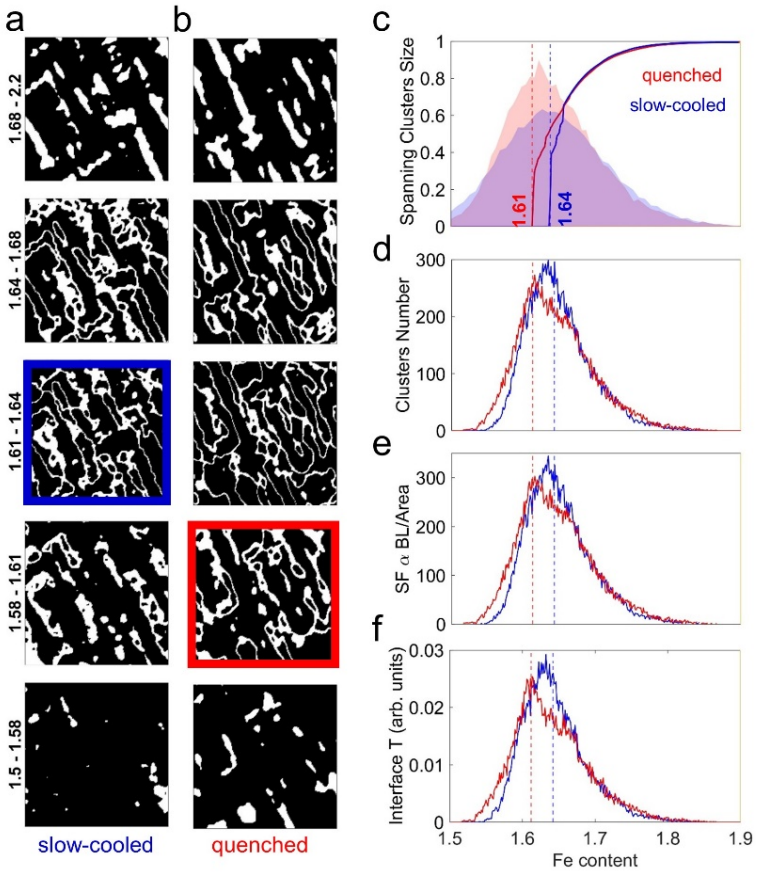

Figure 4. Chemical-structural phase separation coupled with percolation.

Segmented fluorescence maps of Fe content for the slow cooled **(a)** and the quenched **(b)** samples. The Fe fluorescence texture at which phase percolation occur are shown framed for the quenched (red) and the slow cooled (blue) samples. The spanning cluster size in quenched (red continuous line) and slow cooled (blue continuous line) samples is shown in **(c)** together with the Fe fluorescence intensities distributions (shaded areas) already shown in Figure 2. The percolation thresholds, that is the Fe content at which the first spanning cluster forms, are indicated by vertical dashed lines for the slow cooled (blue) and quenched (red) sample. The threshold value for the quenched sample (P_T^{Fe}=1.615) is lower than the one for the slow cooled sample (P_T^{Fe}=1.642). **(d)** Number of forming clusters with their **(e)** shape factor in quenched (red continuous line) and slow cooled (blue continuous line) samples as a function of Fe content. The interface thickness T is shown in **(f)**.

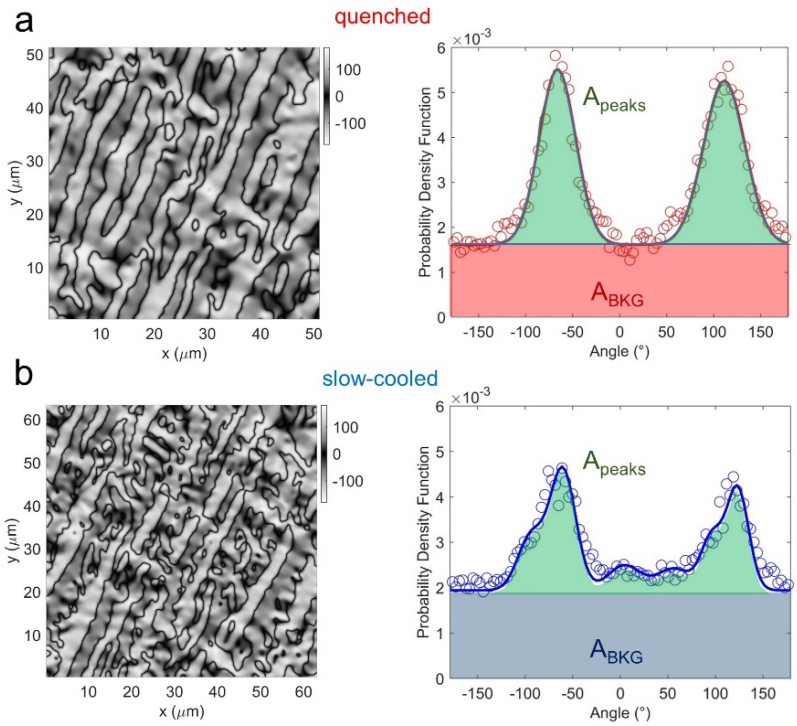

Figure 5. Ordering and inhomogeneity degree controlled by thermal treatments

(Left panels) Gradient orientation maps of the quenched sample with (right panels) the Probability Density Function (PDF) for the quenched **(a)** and slow cooled **(b)** samples. The continuous lines in the PDF plots represent the Gaussian functions fits above a constant background. The preferred direction for the quenched sample is around 120°, while the orientation gradient of the slow cooled sample shows also different secondary orientations around 100°, 0°, 50° beyond the main preferred orientation around 120°. The orientation degree, given by the ratio between the area of the peaks, A_{peaks}, and the Area under the peaks, A_{BKG}, is found to be 0.42 and 0.72 for the slow cooled and for the quenched sample, respectively. We have used the Sobel numerical operator for computing the gradient of the Fe spatial distributions.

Supplementary Information

The spatial correlations of Fe and K distributions show different corelation lengths in the quenched and slow cooled samples (see **Figure SI 2** and **Table 1**), as found by calculating the G(r) function for the Fe and K spatial distribution maps in the two samples. To obtain G(r), we have first calculated the correlations of any pairs of spots in the 2D image separated by the vector $\vec{r} = \vec{R}_i - \vec{R}_j$ in the x-y plane, following the expression:

$$G(\overrightarrow{r}) = \frac{1}{N(\overrightarrow{r})}\sum_{i,j}\delta_{\overrightarrow{r},\overrightarrow{R(i)}-\overrightarrow{R(j)}}\frac{(I_i-\langle I\rangle_1)(I_j-\langle I\rangle_2)}{\sigma_1\sigma_2} \quad (1)$$

where $N(\overrightarrow{r}) = \sum_{i,j}\delta_{\overrightarrow{r},\overrightarrow{R(i)}-\overrightarrow{R(j)}}$ indicates the number of points at distance $\vec{r} = \vec{R}_i - \vec{R}_j$. The average intensities are calculated according to the expressions

$$\langle I\rangle_1 = \frac{1}{N(\overrightarrow{r})}\sum_{i,j}\delta_{\overrightarrow{r},\overrightarrow{R(i)}-\overrightarrow{R(j)}}I_i \quad (2)$$

$$\langle I\rangle_2 = \frac{1}{N(\overrightarrow{r})}\sum_{i,j}\delta_{\overrightarrow{r},\overrightarrow{R(i)}-\overrightarrow{R(j)}}I_j$$

and the standard deviation are calculated according to

$$\sigma_1^2 = \left(\frac{1}{N(\overrightarrow{r})}\sum_{i,j}\delta_{\overrightarrow{r},\overrightarrow{R(i)}-\overrightarrow{r(j)}}I_i^2\right) - \langle I\rangle_1^2 \quad (3)$$

$$\sigma_2^2 = \left(\frac{1}{N(\overrightarrow{r})}\sum_{i,j}\delta_{\overrightarrow{r},\overrightarrow{R(i)}-\overrightarrow{R(j)}}I_j^2\right) - \langle I\rangle_2^2.$$

Finally, we take $G(r) = \langle G(\vec{r})\rangle$ where the average is over all the allowed directions in the grid describing the 2D image. The Fe distribution in the slow cooled sample shows two correlation distances around R_1=14 μm and R_2=26 μm, while we have found only one larger correlation distance, R_1=29 μm in the quenched sample. A scheme to clarify the meaning of the correlation distances is given in **Figure SI 2b**, where the minimum R_1 distance is depicted as the more probable distance occurring between spots with the same Fe content. The K arrangement, occurring in the spots with low Fe content, shows similar G(r) found for the Fe distribution in the slow cooled sample, while multiple correlation distances around 10 μm, 20 μm, 30 μm and 38 μm occur in the quenched sample, indicating a more ordered like-mesh texture.

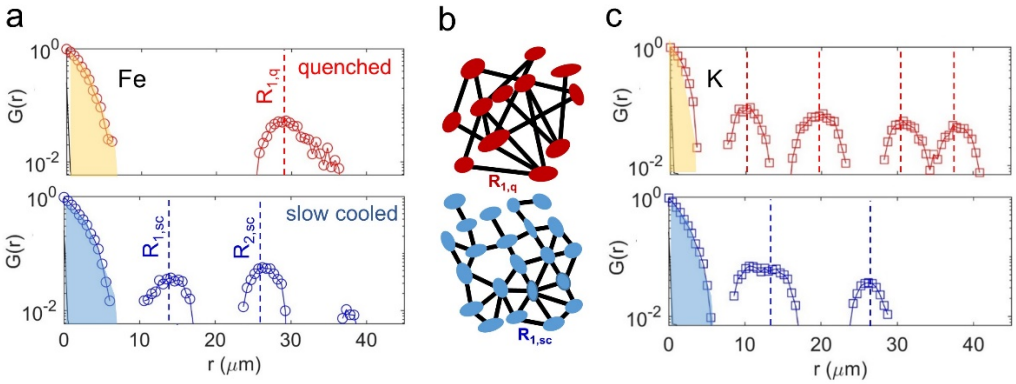

Figure SI 1. Spatial correlations of Fe and K distribution.

(a) G(r) extracted for Fe maps in the (upper panel) quenched and (lower panel) slow cooled samples. The decay of G(r) is related to the mean size of the grain in the map. The peaks in the G(r) represent the correlation distances. The Fe grains are about 5 microns and have correlation distances around $R_{1,sc}$=14 μm and $R_{2,sc}$=26 μm, indicated by the blue vertical dashed lines, in the slow cooled sample. On the other hand, we find only one correlation distance $R_{1,q}$=29 μm for the Fe distribution in the quenched sample. **(b)** Scheme of spatial arrangement of grains with correlation distance equal to R_1, that is the minimum correlation distance found in the quenched (R_1=28μm) and slow cooled sample (R_1=10μm), respectively. **(c)** G(r) extracted for K maps in the (upper panel) quenched and (lower panel) slow cooled samples. Here we find generally shorter correlation distances between smaller K grains in the slow cooled sample. On the other hand in the slow cooled sample, we observe a G(r) not much dissimilar from Fe.

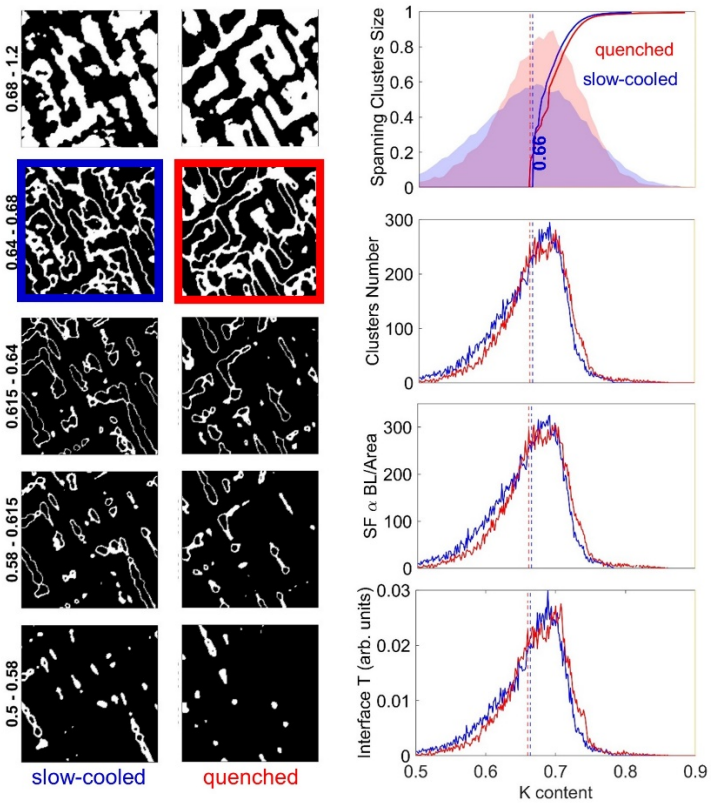

Figure SI 2. Percolation of K clusters.

Binarized maps at different K content values indicated in the slow cooled and quenched samples. The texture of the K content at which percolation occurs are indicated by the red and blue frames for the quenched and the slow cooled samples, respectively. In the right panels, in analogy with Figure 3 for Fe content, we report spanning cluster size, number of forming clusters with their shape factor and the interface T behaviour as a function of K content in (red continuous line) quenched and (blue continuous line) slow cooled samples. The compositional K distribution for the slow cooled and quenched sample, already shown in Figure 2, are also indicated by the blue and red shadowed areas in spanning cluster panel. The percolation thresholds, that is the K content at which the first spanning cluster forms, are indicated by dashed blue and red lines for the slow cooled and quenched sample. We find a similar threshold P_T^k=0.66 for the quenched and the slow cooled samples.

The Euclidean Distance Transform, EDT, gives the distance from each pixel in one phase to the nearest pixel in the other phase [Maurer, 2003]. This method is a common approach to characterize the interface in composites where dispersed minority phase in a host matrix phase plays a crucial role in determining the overall properties of the composite [Wong, 2006; Ender, 2012]. Following this approach, we have defined the evolution of thickness, T, of the interface with the Fe content of the material. In **Figure SI 2a** we visualize the EDT maps at the Fe content at different Fe intervals for the quenched and slow cooled samples.

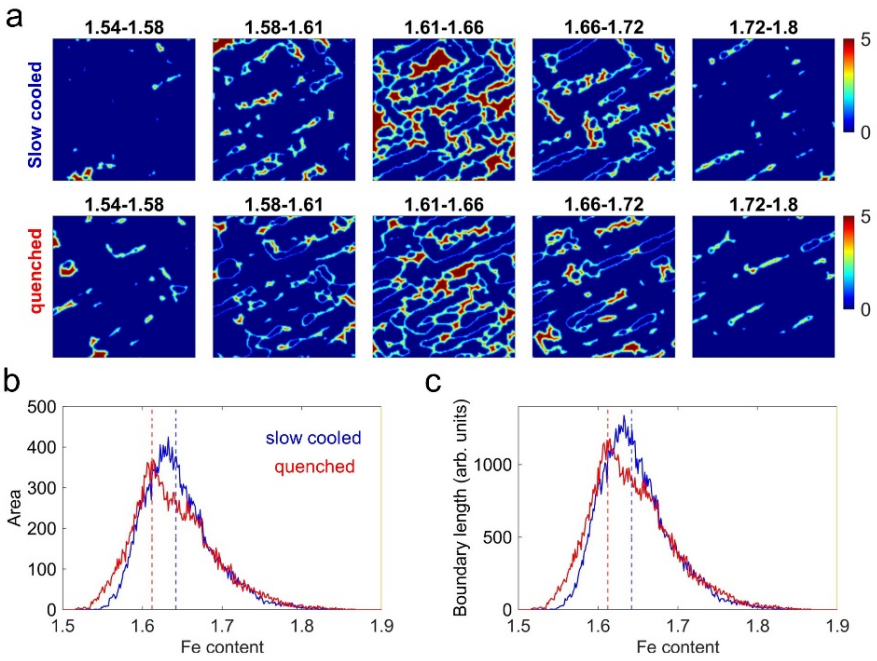

Figure SI 3. Euclidean distance transform: interface between lower and higher Fe density domains

(a) EDT maps at the different indicated Fe contents in the quenched and slow cooled samples. The interface thickness at each Fe content is given by the mean of the EDT map obtained at that specific content. **(b)** Area and **(c)** boundary length of Fe clusters as a function of Fe content.

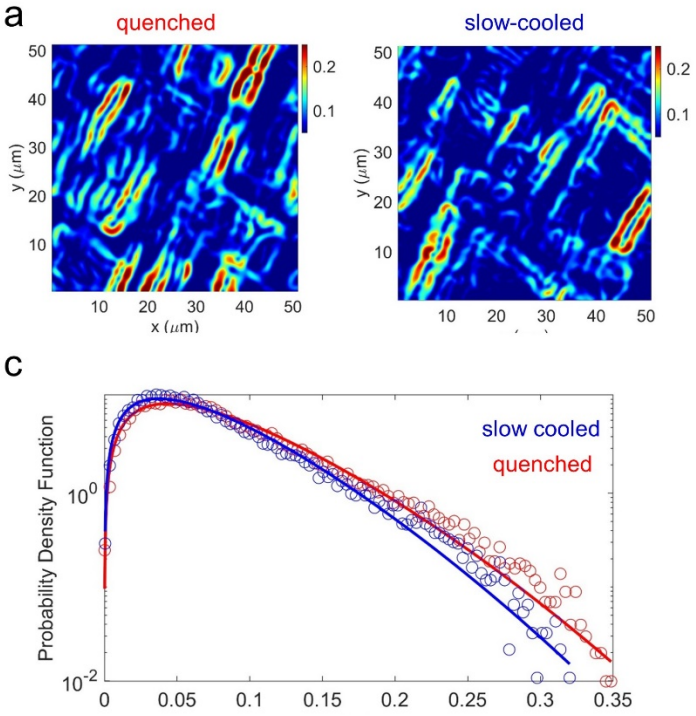

Figure SI 4. Gradient magnitude of Fe content

(a) Maps of gradient magnitude and **(b)** Probability Density Function of Fe content in the quenched and slow cooled samples.

Surface metallic/insulating texture has been investigated by Scanning Photoemission Microscopy (SPEM) measurements. The maps of the photoelectron yield at E_F are plotted together with representative photoemission spectra in **Figure 5a SI** and **Figure 5b SI** for the slow cooled and the quenched samples, respectively. The difference between insulating and metallic phases are well depicted and we can resolve metallic and insulating domains in both quenched and slow cooled samples. We interpret the photoemission microscopy images as representative of the topmost part of the metallic and insulating domains, whose thickness cannot be comparable to the XRF probing depth. Anyway, this penetration depth provides excellent agreement with XRF imaging in the case of the slow cooled sample. On the other hand, the surface morphology of the metallic domains appears quite different from the bulk Fe organization observed in the quenched sample. The different spatial distribution of metallicity in **Figure 6c** show a fatter tail in the slow cooled sample due to surface domains with larger metallicity.

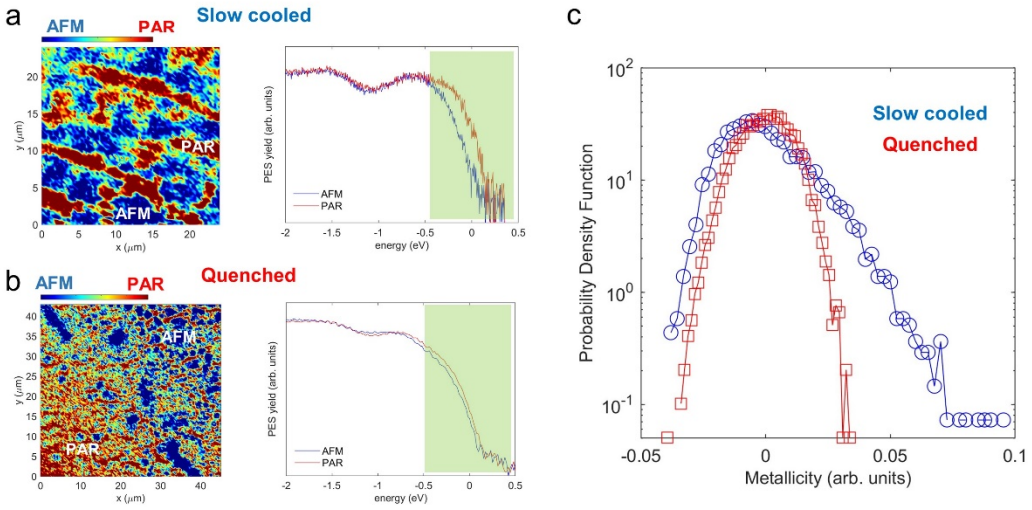

Figure SI 5. Scanning photoemission microscopy

Scanning photoemission microscopy maps and spectra on **(a)** quenched and **(b)** slow cooled samples, collected at 27 eV photon energy at room temperature. The images are obtained with standard procedures to remove background. The pictorial contrast between metallic (PAR) and insulating (AFM) zones is obtained from the photoemission intensity integrated in a range of 1 eV around at the Fermi level (green area in the right panels), normalized by the intensity of the photoemission profiles on the whole energy range (binding energy = 23.3 eV). The variation of this normalized intensity is represented in the same colour scale for the two maps from its minimum value, AFM phase in blue, to its maximum, PAR phase in red. Therefore, this is a direct visualization in real space of the metallicity of the system where metallic (in red) and insulating (in blue) domains coexist. The photoemission spectra (right panels) are the averaged spectra on selected representative areas in the photoemission maps. **(c)** Probability Density Function of the photoemission intensity in the (blue circles) slow cooled and in the (red circles) quenched samples. The different spatial distribution of metallicity showing a clear fatter tail in the slow cooled sample is due to domains with larger metallicity.

References

Skolnick, M., & Torquato, S. (2024). Quantifying phase mixing and separation behaviors across length and time scales. Acta Materialia, 119774.

Wen, H. H. (2000). Macroscopic phase separation in high-temperature superconductors. *Proceedings of the National Academy of Sciences*, *97*(21), 11145-11146.

Fine, B. V., & Egami, T. (2008). Phase separation in the vicinity of quantum-critical doping concentration: Implications for high-temperature superconductors. *Physical Review B*, *77*(1), 014519.

Campi, G., Ricci, A., Poccia, N., Barba, L., Arrighetti, G., Burghammer, M., ... & Bianconi, A. (2013). Scanning micro-x-ray diffraction unveils the distribution of oxygen chain nanoscale puddles in YBa2Cu3O6.33. *Physical Review B*, *87*(1), 014517.

Campi, G., & Bianconi, A. (2021). Functional nanoscale phase separation and intertwined order in quantum complex materials. Condensed Matter, 6(4), 40.

Yan, Y. J., Zhang, M., Wang, A. F., Ying, J. J., Li, Z. Y., Qin, W., ... & Chen, X. H. (2012). Electronic and magnetic phase diagram in KxFe2-ySe2 superconductors. *Scientific Reports*, *2*(1), 212.

Ricci, A., Poccia, N., Joseph, B., Innocenti, D., Campi, G., Zozulya, A., ... & Saini, N. L. (2015). Direct observation of nanoscale interface phase in the superconducting chalcogenide K x Fe 2− y Se 2 with intrinsic phase separation. Physical Review B, 91(2), 020503.

Ricci, A., Campi, G., Joseph, B., Poccia, N., Innocenti, D., Gutt, C., ... & Saini, N. L. (2020). Intermittent dynamics of antiferromagnetic phase in inhomogeneous iron-based chalcogenide superconductor. Physical review B, 101(2), 020508.

Shoemaker, D. P., Chung, D. Y., Claus, H., Francisco, M. C., Avci, S., Llobet, A., & Kanatzidis, M. G. (2012). Phase relations in KxFe2−ySe2 and the structure of superconducting KxFe2Se2 via high-resolution synchrotron diffraction. Physical Review B, 86(18), 184511.

Louca, D., Park, K., Li, B., Neuefeind, J., & Yan, J. (2013). The hybrid lattice of KxFe2− ySe2: where superconductivity and magnetism coexist. Scientific reports, 3(1), 2047.

Li, W., Ding, H., Deng, P., Chang, K., Song, C., He, K., ... & Xue, Q. K. (2012). Phase separation and magnetic order in K-doped iron selenide superconductor. Nature Physics, 8(2), 126-130.

Yan, Y. J., Zhang, M., Wang, A. F., Ying, J. J., Li, Z. Y., Qin, W., ... & Chen, X. H. (2012). Electronic and magnetic phase diagram in KxFe2-ySe2 superconductors. Scientific reports, 2(1), 1-5.

Chen, Y., Jiang, J., Yang, H., Dudin, P., Barinov, A., Liu, Z., ... & Chen, Y. (2021). Visualization of the electronic phase separation in superconducting KxFe2−ySe2. Nano Research, 14, 823-828.

Simonelli, L., Mizokawa, T., Sala, M. M., Takeya, H., Mizuguchi, Y., Takano, Y., ... & Saini, N. L. (2014). Temperature dependence of iron local magnetic moment in phase-separated superconducting chalcogenide. Physical Review B, 90(21), 214516.

Yanagisawa, Y., Tanaka, M., Yamashita, A., Suzuki, K., Hara, H., ElMassalami, M., ... & Takano, Y. (2017). Phase-Separation Control of KxFe2−ySe2 Superconductor through Rapid-Quenching Process. Journal of the Physical Society of Japan, 86(4), 043703.

Zheng, S. T., Wang, J. F., Li, W., He, C., Zhang, Z., Li, L., ... & Zhang, Y. (2012). Phase separation and its enhanced superconductivity in K-doped iron selenide single crystals. Scientific Reports, 2(1), 1-6.

Ding, X., Fang, D., Wang, Z., Yang, H., Liu, J., Deng, Q., ... & Wen, H. H. (2013). Influence of microstructure on superconductivity in K x Fe2− y Se2 and evidence for a new parent phase K2Fe7Se8. Nature Communications, 4(1), 1897.

Abd Mutalib, M., Aziz, F., Ismail, A. F., Salleh, W. N. W., Yusof, N., Jaafar, J., ... & Ludin, N. A. (2018). Towards high performance perovskite solar cells: a review of morphological control and HTM development. Applied Materials Today, 13, 69-82.

Ma, Q., & Zhang, Y. (2016). Mechanics of fractal-inspired horseshoe microstructures for applications in stretchable electronics. Journal of Applied Mechanics, 83(11).

Yanagisawa, Y., Tanaka, M., Yamashita, A., Suzuki, K., Hara, H., ElMassalami, M., ... & Takano, Y. (2017). Phase-Separation Control of K x Fe2− y Se2 Superconductor through Rapid-Quenching Process. Journal of the Physical Society of Japan, 86(4), 043703.

Taylor, J. (2016). Heavy-tailed Distributions. Retrieved December 10, 2017 from: https://math.la.asu.edu/~jtaylor/teaching/Spring2016/STP421/lectures/stable.pdf

Nair, J., Wierman, A., & Zwart, B. (2022). The fundamentals of heavy tails: Properties, emergence, and estimation (Vol. 53). Cambridge University Press.

Campi, G., Di Gioacchino, M., Poccia, N., Ricci, A., Burghammer, M., Ciasca, G., & Bianconi, A. (2017). Nanoscale correlated disorder in out-of-equilibrium myelin ultrastructure. ACS nano, 12(1), 729-739.

Klebanov, L. B., Kuvaeva-Gudoshnikova, Y. V., & Rachev, S. T. (2023). Heavy-tailed probability distributions: Some examples of their appearance. Mathematics, 11(14), 3094.

Su, C., & Tang, Q. (2004). Heavy-tailed distributions and their applications. In Probability, Finance And Insurance (pp. 218-236).

Kotz, S., & Nadarajah, S. (2000). Extreme value distributions: theory and applications. world scientific.

Yeh, K. Y., Chen, Y. R., Lo, T. S., Wu, P. M., Wang, M. J., Chang-Liao, K. S., & Wu, M. K. (2020). Fe-vacancy-ordered Fe4Se5: The insulating parent phase of FeSe superconductor. Frontiers in Physics, 8, 567054.

Kirch, W. (Ed.). (2008). Encyclopedia of Public Health: Volume 1: A-H Volume 2: I-Z. Springer Science & Business Media.

Duan, C., Yang, J., Ren, Y., Thomas, S. M., & Louca, D. (2018). Appearance of superconductivity at the vacancy order-disorder boundary in K x Fe 2− y Se 2. Physical Review B, 97(18), 184502.

Stauffer, D. & Aharony, A. Introduction to Percolation Theory (Taylor and Francis, 1994).

Zhou, J., Odqvist, J., Thuvander, M., Hertzman, S., & Hedström, P. (2012). Concurrent phase separation and clustering in the ferrite phase during low temperature stress aging of duplex stainless steel weldments. Acta Materialia, 60(16), 5818-5827.

Mendelson, K. S. (1999). Percolation threshold of correlated two-dimensional lattices. Physical Review E, 60(6), 6496.

Maurer, Calvin, Rensheng Qi, and Vijay Raghavan, "A Linear Time Algorithm for Computing Exact Euclidean Distance Transforms of Binary Images in Arbitrary Dimensions," IEEE Transactions on Pattern Analysis and Machine Intelligence, Vol. 25, No. 2, February 2003, pp. 265-270.

Wong, H. S., & Buenfeld, N. R. (2006). Euclidean distance mapping for computing microstructural gradients at interfaces in composite materials. Cement and Concrete Research, 36(6), 1091-1097.

Ender, M., Joos, J., Carraro, T., & Ivers-Tiffée, E. (2012). Quantitative characterization of LiFePO4 cathodes reconstructed by FIB/SEM tomography. Journal of the electrochemical society, 159(7), A972.

Gonzales, R. C., & Wintz, P. (1987). Digital image processing. Addison-Wesley Longman Publishing Co., Inc.

Poccia, N., Zhao, S. Y. F., Yoo, H., Huang, X., Yan, H., Chu, Y. S., ... & Kim, P. (2020). Spatially correlated incommensurate lattice modulations in an atomically thin high-temperature Bi2.1Sr1.9CaCu2.0O8+y superconductor. Physical Review Materials, 4(11), 114007.

Park, J. Y., Han, K. S., Woo, J. S., Chang, S. K., Rajmohan, N., & Szpunar, J. A. (2002). Influence of primary annealing condition on texture development in grain oriented electrical steels. Acta Materialia, 50(7), 1825-1834.

Liu, Y., Xing, Q., Straszheim, W. E., Marshman, J., Pedersen, P., & Lograsso, T. A. (2015). In situ observation of phase separation and hierarchical microstructure of KxFe2-ySe2 single crystals. arXiv preprint arXiv:1502.04335.

Cotte, M., Pouyet, E., Salomé, M., Rivard, C., De Nolf, W., Castillo-Michel, H., ... & Susini, J. (2017). The ID21 X-ray and infrared microscopy beamline at the ESRF: status and recent applications to artistic materials. Journal of Analytical Atomic Spectrometry, 32(3), 477-493.

Campi, G., & Bianconi, A. (2019). Evolution of complexity in out-of-equilibrium systems by time-resolved or space-resolved synchrotron radiation techniques. Condensed Matter, 4(1), 32.

Tanaka, M., Yanagisawa, Y., Denholme, S. J., Fujioka, M., Funahashi, S., Matsushita, Y., ... & Takano, Y. (2016). Origin of the Higher-T c Phase in the K x Fe2− y Se2 System. Journal of the Physical Society of Japan, 85(4), 044710.